Particle-in-cell simulations of burning inertial confinement fusion capsule implosions

Johannes J. van de Wetering,* Justin R. Angus, W. Farmer, V. Geyko, D. Ghosh, D. Grote, C. Weber, and G. Zimmerman

Lawrence Livermore National Laboratory, Livermore, California 94551, USA

(Received 4 June 2025; accepted 17 September 2025; published 9 October 2025)

Anomalies observed in the neutron spectral shift of high-yield shots at the National Ignition Facility (NIF) suggest the presence of suprathermal ions [E. P. Hartouni *et al.*, Nat. Phys. **19**, 72 (2023)], implying that kinetic effects play a significant role in burning inertial confinement fusion (ICF) plasmas. Furthermore, recent measurements of reaction-in-flight (RIF) neutrons offer a direct probe of the stopping power in the burning fuel region of high-energy alpha particles and up-scattered fuel ions. We have developed the particle-in-cell code PICNIC, an *exactly* energy-conserving particle-in-cell Monte-Carlo collision (PIC-MCC) code to simulate the burn stage in ICF. We present results from 1D spherical simulations of NIF shot N210808, which was the first to exceed the Lawson criterion for laser fusion. We find that the suprathermal ions generated by large-angle Rutherford and nuclear elastic scattering (NES) with fusion alphas produce an alpha knock-on neutron (AKN) signal consistent with the extent and relative yield of the AKN spectrum identified in ignition experiments at the NIF. We also find that the inclusion of large-angle scattering physics does not explain the anomalously large spectral shift observed in the experiment.

DOI: 10.1103/zwjx-jbxl

I. INTRODUCTION

Ever since the first ignition result at the National Ignition Facility (NIF) [1,2], the NIF has provided access to the burning plasma regime with ever-increasing yields [3], opening new research avenues to further optimize yield. For instance, recent measurements of the neutron spectra of burning inertial confinement fusion (ICF) implosions have exhibited anomalously large spectral shifts in the D–T primary spectrum beyond what is expected from a purely thermonuclear plasma [4,5]. This observation suggests the presence of a significant population of suprathermal fuel ions and highlights the importance of understanding kinetic effects in this regime.

Furthermore, in burning D/T plasmas, it is known that large-angle elastic scattering of alpha particles against thermal D/T fuel ions generates suprathermal ion populations, leading to significant modifications to the emitted neutron spectrum and can influence overall yield [6–14]. A spectral feature of particular interest is the high-energy reaction-in-flight (RIF) alpha knock-on neutron (AKN) tail in the 15.5–18 MeV range, which has been proposed to serve as a direct probe of hotspot conditions and stopping powers of alphas and suprathermal fuel ions in the partially degenerate burning plasmas in ICF implosions [15–17].

Previous efforts in capturing kinetic effects in ICF include ion Vlasov-Fokker-Planck (iVFP) simulations [18–20], with comparisons to ICF experiments below the ignition threshold at the OMEGA laser facility [21], which can capture non-hydrodynamic effects like thermal decoupling, multi-species separation, and ion diffusion. However, in moderately coupled burning plasmas where the large mean-free-path, short-range, large-angle scattering of alphas against D/T determines the high-energy tail of the neutron spectrum, particle transport departs from the pure Fokker-Planck picture and enters a mixed regime with Boltzmann-like transport, necessitating a more complete kinetic model.

The particle-in-cell (PIC) code PICNIC is used in this work to investigate the role of kinetic effects during the burn phase in ICF capsule implosions [22,23], with simulations initialized ∼150 ps before bangtime including the hotspot, D/T ice, and carbon liner. In this paper, we first give an overview of the physics modules included in PICNIC used in this work. We then provide a brief discussion of neutron spectra in ICF and the components we include in our study. Finally, we present 1D spherical simulation results of the full burn phase of NIF shot N210808.

II. METHODS

PICNIC is a fully implicit, *exactly* energy-conserving, electromagnetic and relativistic PIC-Monte-Carlo collision (PIC-MCC) code that supports planar, 1D/2D cylindrical, and 1D spherical geometries [23]. For all scattering routines, PICNIC uses a moment-preserving MCC method that maintains the correct scattering physics between particles of different weights while preserving local momentum and energy conservation [24]. This method is especially necessary for problems in spherical geometry with non-local transport (e.g., alpha heating) where macroparticle weights can strongly vary within a cell.

A. Coulomb scattering

The Coulomb collision module includes both cumulative small-angle and single large-angle Rutherford scattering for

*Contact author: vandeweterin1@llnl.gov

moderately coupled plasmas [25,26], which builds upon the work by Turrell [27] and uses the quantum mechanical impact parameter corrections derived in [28]. The inclusion of large-angle Rutherford scattering physics is necessary to yield the Li-Petrasso $\sim 1/\ln\Lambda$ corrections to the Fokker-Planck collision operator [29] in the moderately coupled plasmas $2 \lesssim \ln\Lambda \lesssim 10$ relevant to ICF implosions [30,31]. Single large-angle Rutherford scattering also contributes to the generation of suprathermal ions in burning plasmas, though it is superseded by nuclear elastic scattering (NES) in the relevant multi-MeV energy range [7,9,32,33].

B. Radiation

For radiative transport of X-rays generated by the burning plasma, we have implemented a 3D ray-tracing bremsstrahlung and inverse bremsstrahlung model, building upon the work by Lavell [34], which uses the Seltzer-Berger cross section tables [35]. Our implementation differs in a few key ways: For bremsstrahlung emission, we also include the (weighted) ion recoil to simultaneously conserve energy and momentum, rather than only considering the electron as in [34], which conserves energy but not momentum. For inverse bremsstrahlung, we use another simultaneously energy- and momentum-conserving method which distributes the absorbed photon energy and momentum amongst all the electrons in a cell, similar to the implementation of the moment-preserving collision method for weighted particles [24].

In addition, we use a cutoff frequency set by the plasma frequency ω_p in the cell, and we apply a dynamic group velocity of the photon macroparticles set by $v_g/c = (1-\omega_p^2/\omega^2)^{1/2}$ for more accurate radiation transport. For simplicity, we do not consider refraction of the rays.

C. Nuclear elastic scattering

Nuclear elastic scattering (NES) refers to the strong force-mediated interaction X(Y,Y')X', where X' denotes the recoil of the nucleus X against Y, which both remain in the ground state. Specifically for the single large-angle collisions relevant to multi-MeV suprathermal ion production, NES generally has a cross section roughly one to two orders of magnitude larger than that of Rutherford scattering [7] and is therefore important to consider for burning D/T plasmas. To include the effects of NES, we follow the approach outlined in [9], where the total differential cross section is written as a sum of the pure Rutherford cross section and a nuclear interference term

$$\frac{d\sigma}{d\Omega} = \frac{d\sigma_C}{d\Omega} + \frac{d\sigma_{NI}}{d\Omega}. \tag{1}$$

The Rutherford cross-section always dominates at shallow angles, which is already handled by the Coulomb collision algorithm. A minimum cutoff angle of $\theta_{min} = \max(\theta_0, 20^\circ)$ is chosen as per the procedure in [9], where θ_0 is the largest root of the nuclear interference term, to ensure positivity of the nuclear interference term while maintaining sufficient accuracy for the large-angle collisions relevant to suprathermal ion generation.

To model AKN, we have implemented NES for α–D and α–T using the Okhrimovskyy method for anisotropic elastic scattering [36] by calculating the total and transport cross sections of the nuclear interference term using the differential cross section tables from the DRESS code [32]. These tables are based on the optical model for nuclear interference scattering in [9]. On top of the scattering with alphas, we also include NES between D–T following the same procedure using differential cross sections from the ENDF/B-VIII library [33] for its contribution to the stopping of up-scattered fuel ions.

D. Nuclear fusion

The fusion reactions we consider in our simulations are D–T, D–D, T–T, and D–^{3}He using the parameterized cross sections from Bosch and Hale [37]. We have also implemented the method presented in [38] to capture the anisotropy of the D–T and D–D fusion reactions. For simplicity, we treat D–^{3}He fusion as isotropic. For T–T fusion, we use a Monte-Carlo implementation of the Lacina model [39], which accounts for the neutron-neutron interaction in the ^{4}He +n + n channel. We choose to neglect the two ^{5}He +n channels as they are only a perturbative effect for the bulk $\sim$10 keV reactant energies in ICF [40].

III. ICF NEUTRON SPECTRUM

A. D–T primary spectrum

The shift and variance of the spectral D–T neutron peak are measured to infer the yield-averaged ion temperature and relative kinetic energy between the reactants. The spectral

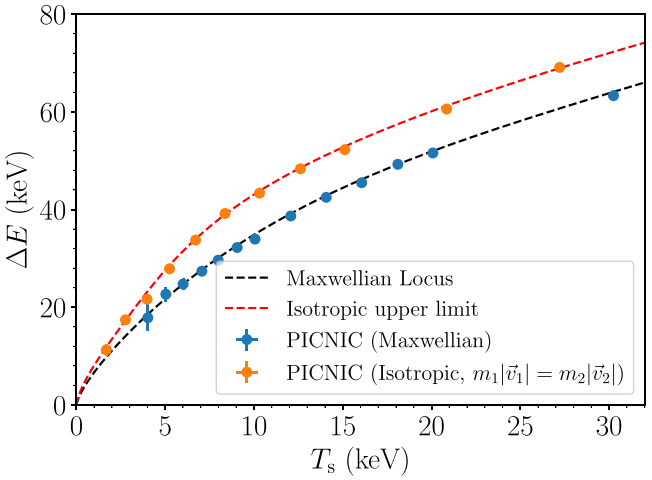

FIG. 1. Verification of the neutron spectra generated by the fusion algorithm implemented in PICNIC. The D–T neutron spectral shift and variance from simulations are compared with the Maxwellian locus and the isotropic distribution upper limit derived in [43] and [42], respectively. The isotropic upper limit corresponds to monoenergetic, momentum-matched distributions. Isotropic distributions (e.g., thermal Maxwellians) can only access the $T_s - \Delta E$ region underneath this curve. Simulations were performed on a 2D 10×10 grid with $N^D_{ppc} = N^T_{ppc} = 16384$ and were run for a single timestep to prevent time-variation of the particle distributions. The spectral temperature T_s was recovered using the sample variance of the neutrons. Particle motion and forces were turned off, making each simulation an average of 100 independent 0D (velocity space only) realizations.

shift is measured relative to the neutron energy at zero reaction energy $E_0 = 14.0284$ MeV

$$\Delta E = \langle E_n \rangle - E_0, \tag{2}$$

where $\langle \ldots \rangle$ denotes averaging over the total D–T neutron yield. The variance is directly related to the ion temperature via Doppler broadening [41], with the spectral ion temperature defined as [42]

$$T_s = \frac{m_D + m_T}{3\beta_0} \mathrm{Var}(E_n), \tag{3}$$

where $\beta_0 = 8852.7\ \mathrm{MeV}^2/c^2$. Given the distribution functions of the fuel ions, and assuming a steady state, there is a direct relation between the spectral shift and variance. For the special case of Maxwellian distribution functions, the relativistically correct relation between ΔE and T_s was derived by Ballabio [43] and is shown in Fig. 1, where it is compared with PICNIC simulation results recovering the same curve. This curve is often referred to as the "hydrodynamic limit," as any points that fall below it are accessible by Maxwellian plasmas with varying bulk fluid velocity Doppler shifts, which increase the spectral variance. Spectra found above this curve, as reported in [4,5], would then be evidence of kinetic effects producing a specific class of non-Maxwellian distributions that produce larger spectral shifts. We also show in the same figure that PICNIC reproduces the upper limit curve accessible by isotropic distributions derived in [42], which indicates the largest possible spectral shift accessible by isotropic velocity distributions.

B. Reaction-in-flight neutrons

RIF neutrons are produced in a 3-step process [44]. First, D–T fusion occurs between thermal ions, producing on an average 3.54 MeV alphas and 14.1 MeV neutrons. Then, either the alphas or neutrons can "knock-on" D or T fuel ions by undergoing a large-angle elastic scatter. This generates a suprathermal D/T population which can then undergo fusion reactions with the thermal D/T in-flight, producing higher-energy RIF neutrons. The kinematic limits of alpha knock-on and neutron knock-on (NKN) neutrons are summarized as follows [16]:

$$\begin{aligned}
&\alpha(3.5\ \mathrm{MeV}) \rightarrow \mathrm{T}(\leqslant 3.4\ \mathrm{MeV}) + \mathrm{D} \rightarrow \mathrm{n}(10.6\text{–}20.6\ \mathrm{MeV}), \quad \alpha(3.5\ \mathrm{MeV}) \rightarrow \mathrm{D}(\leqslant 3.1\ \mathrm{MeV}) + \mathrm{T} \rightarrow \mathrm{n}(11.9\text{–}19.7\ \mathrm{MeV}),\\
&\mathrm{n}(14.1\ \mathrm{MeV}) \rightarrow \mathrm{T}(\leqslant 10.5\ \mathrm{MeV}) + \mathrm{D} \rightarrow \mathrm{n}(9.3\text{–}28.1\ \mathrm{MeV}), \quad \mathrm{n}(14.1\ \mathrm{MeV}) \rightarrow \mathrm{D}(\leqslant 12.4\ \mathrm{MeV}) + \mathrm{T} \rightarrow \mathrm{n}(12.1\text{–}30\ \mathrm{MeV}).
\end{aligned} \tag{4}$$

The AKN part of the spectrum for ignited capsules is the dominant RIF signal in the 15.5–18 MeV range, where the contributions from the Doppler-broadened D–T peak and NKN are smaller. This has led the AKN signal to be proposed as a direct probe for the alpha stopping power within the fuel during the burn [15].

C. Triton burn-up neutrons

D–D fusion occurs via two equally likely branches whose products can lead to secondary fusion reactions

$$\mathrm{D} + \mathrm{D} \rightarrow \mathrm{T}(1.01\ \mathrm{MeV}) + \mathrm{p}(3.02\ \mathrm{MeV}), \quad \mathrm{D} + \mathrm{D} \rightarrow {}^3\mathrm{He}(0.82\ \mathrm{MeV}) + \mathrm{n}(2.45\ \mathrm{MeV}). \tag{5}$$

Aside from directly introducing a spectral peak at 2.45 MeV via the $^3\mathrm{He} + \mathrm{n}$ channel, the T + p channel adds to the tails of the primary D–T spectrum with the emitted 1.01 MeV tritons. As these high-energy tritons react with thermal deuterons, they produce "triton burn-up" (TBN) neutrons that appear in the neutron spectrum in the following energy range (in the absence of thermal broadening)

$$\mathrm{T}(\leqslant 1.01\ \mathrm{MeV}) + \mathrm{D} \rightarrow \mathrm{n}(11.8\text{–}17.1\ \mathrm{MeV}). \tag{6}$$

Note that while this is the dominant non-Maxwellian signal for low-yield shots [44], for high-yield ignition shots, the TBN signal is drowned out by the RIFs by roughly an order of magnitude.

D. T–T spectrum

The kinematics of tritium-tritium fusion is complicated by its release of three products, allowing for a spectrum of possible product energies in the center-of-momentum frame. The T–T fusion reaction can follow three separate channels

$$\begin{aligned}
&\mathrm{T} + \mathrm{T} \rightarrow {}^4\mathrm{He} + \mathrm{n} + \mathrm{n}, \quad Q = 11.3\ \mathrm{MeV},\\
&\mathrm{T} + \mathrm{T} \rightarrow {}^5\mathrm{He} + \mathrm{n}, \quad Q_1 = 10.4\ \mathrm{MeV} \rightarrow {}^4\mathrm{He} + \mathrm{n} + \mathrm{n},\\
&\mathrm{T} + \mathrm{T} \rightarrow {}^5\mathrm{He}^* + \mathrm{n}, \quad Q_1 = 9.2\ \mathrm{MeV} \rightarrow {}^4\mathrm{He} + \mathrm{n} + \mathrm{n}.
\end{aligned} \tag{7}$$

The first nontrivial treatment for the kinematics of the first channel is the Lacina model [39], which accounts for the neutron-neutron interaction, treating it as a square-well interaction of 2.5 fm range and −14.3 MeV depth. This skews what would otherwise be an elliptical 0–9.4 MeV T–T neutron spectrum towards lower energies and likewise skews the emitted alpha particle towards higher energies up to a maximum of 3.77 MeV. For simplicity, this is the model we have opted

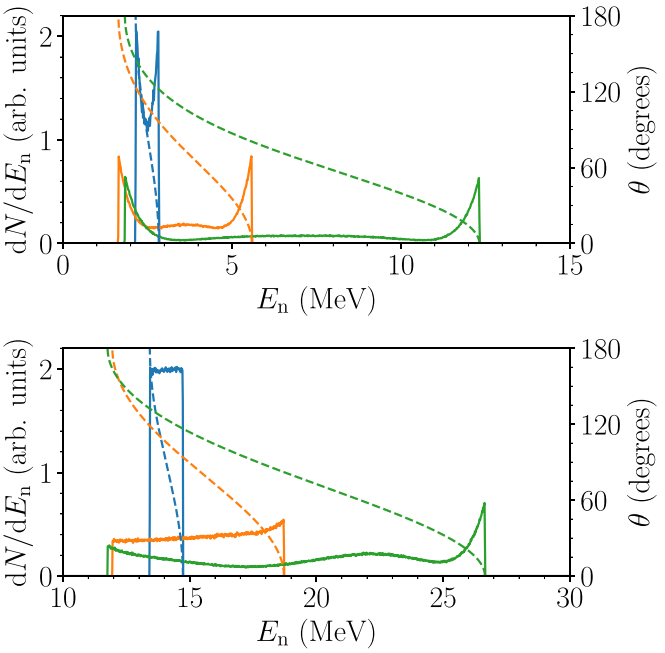

FIG. 2. Anisotropic neutron spectra (solid) and emission angle (dashed) from 0D cold beam-target fusion simulations for (top) D–D and (bottom) D–T. The deuteron beam proper velocities (blue, orange, green) are $u/c = 1\%$, 5%, and 10%, which correspond to projectile energies of 93 keV, 2.3 MeV, and 9.3 MeV respectively.

to implement in this work, as our primary interest lies in the high-energy neutron spectrum.

The α-neutron interaction(s), which we have not included in our calculations, introduces a peak at 8.7 MeV and a corresponding low-energy peak, as well as a reduction in skew of the spectrum. Experimental work at the NIF and more recently at the OMEGA laser facility has demonstrated that this peak is both present [45,46] and sensitive to reactant center-of-mass energy at ICF-relevant ion temperatures [46]. The full description of T–T fusion kinematics remains an active area of research.

E. Fusion anisotropy

The RIF neutron spectrum is also affected by the anisotropy of D–T fusion at high energies. For reactant energies above ∼1 MeV, the emitted neutron becomes increasingly forward-biased with the incident deuteron in the center-of-momentum frame. This results in up-scattered deuterons reacting with a thermal triton having an increased likelihood of emitting upshifted neutrons, while up-scattered tritons reacting with a thermal deuteron tend to emit downshifted neutrons. Hence, the high-energy end of the AKN signal and the NKN signal will receive a larger contribution from the up-scattered deuterons and a reduced contribution from the up-scattered tritons. The neutron emission anisotropy is demonstrated in Fig. 2, which displays the laboratory frame neutron spectra of D–D and D–T beam-target fusion from PICNIC simulations with the implementation described in [38] using the 2015 IAEA evaluation of the differential cross section [47].

IV. 1D SPHERICAL SIMULATION RESULTS OF SHOT N210808

We present the results of three simulations in 1D spherical geometry with the following scattering physics:

(1) cumulative Coulomb + isotropic fusion,

(2) cumulative Coulomb + large-angle Rutherford + α–D/α–T NES + isotropic fusion,

(3) cumulative Coulomb + large-angle Rutherford + α–D/α–T/D–T NES + anisotropic D–D and D–T fusion.

Bremsstrahlung and inverse bremsstrahlung were included in all three simulations. The simulations were initialized at approximately 150 ps before bangtime using density, temperature and implosion velocity profiles from 1D spherical HYDRA [48,49] simulations of shot N210808 including the hotspot, D/T ice and carbon liner, shown in Fig. 3. This time was chosen to be sufficiently early before significant alpha heating occurs, while also already being hot enough to avoid having to account for degeneracy effects which can reduce the alpha stopping power [50]. We also assume that the D/T plasma at this stage is fully ionized in both the hotspot and the ice layer.

As for the numerical setup, we use a uniform radial grid resolution of $\Delta r = 120\,\mu\text{m}/1728 = 69.4\,\text{nm}$, treating $r = 120\,\mu\text{m}$ as an open boundary. We also use a timestep of $\Delta t = 0.1\,\text{fs}$. We found this timestep sufficient in resolving the relevant collisional physics [25]. The number of particles per cell profiles of each species at initialization is also given in Fig. 3, with the total number of e/D/T/^{12}C macroparticles at initialization being 7.4×10^6. For simplicity, the ionization states of all ion species were fixed, with fully ionized D/T and doubly ionized ^{12}C. Neglecting the Carbon ionization physics is acceptable for these simulations as the liner primarily acts to provide inertia to confine the D/T plasma.

The numerical energy conservation is shown in Fig. 4, demonstrating that the total energy conservation violation is several orders of magnitude smaller than the kinetic energies of the relevant species. We also use a simple particle splitting routine, which periodically checks for macroparticles with weights 4× larger than the average in the cell (for cells with at least 20 macroparticles present) and splits them such that the new particle weights approximately match the cell average. We found this to be sufficient to prevent the comparatively mobile electrons from higher-weight regions from forming a non-physical sheath build-up at the origin, which inherently has low particle statistics in 1D spherical geometry. We did not find it necessary to use a particle merging algorithm for these simulations.

Neutron scattering is neglected in an effort to isolate the AKN signal and to avoid downscattered neutron noise in the low energy part of the spectrum, allowing us to also observe its possible effects on the D–D and T–T at-birth neutron spectra (as the fusion cross sections of D–T, D–D, and T–T are all comparable in the ∼1 MeV range). We note that doing so forgoes both NKN and heating effects from neutrons depositing a portion of their energy in the plasma [51,52].

A comparison of the fusion production rates with HYDRA is shown in Fig. 5. Between the PIC simulations, we do not see

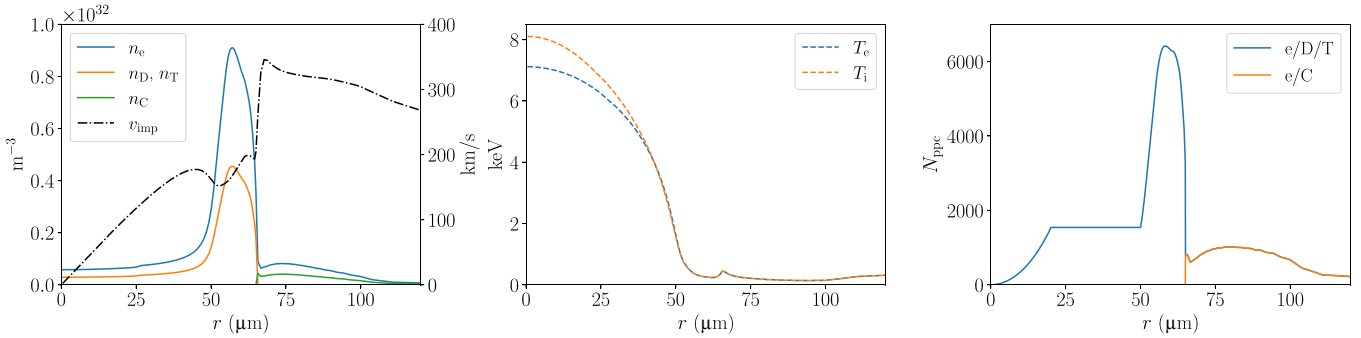

FIG. 3. Initialization profiles for density, temperature, fluid implosion velocity, and number of macroparticles per cell of each species.

any measurable differences in the yields with or without the inclusion of large-angle scattering physics in this regime, and only arguably see a slight reduction in yield with the inclusion of anisotropic fusion. Initially, the PIC simulations have the same production rate as HYDRA. However, once alpha heating becomes relevant at around stagnation, the PIC fusion production rates begin to differ from HYDRA, resulting in a delayed bangtime. The HYDRA simulation has a yield of 2.1 MJ in this time window, while PICNIC simulations (i), (ii), and (iii) have yields of 2.45, 2.44, and 2.35 MJ, respectively. Note that both the HYDRA and PICNIC yields are higher than the reported experimental yield of 1.37 MJ [2] as they are both in 1D spherical geometry and do not take 3D hydrodynamic mixing into account. Determining whether this difference in yield between PICNIC and HYDRA is a kinetic signature is subject to future work, as it requires a detailed comparison of the radiation, alpha stopping, and other forms of heat transport between PICNIC and HYDRA. To highlight the sensitivity to both the radiation emission and absorption models, we also include fusion production rate curves in Fig. 5 of two extra runs of simulation (ii), one without radiation physics, which burns too hot, and the other with radiation but no absorption, which quickly quenches the reaction.

We compare the time evolution of the density, temperature, and pressure profiles between PICNIC and HYDRA in Fig. 6, which qualitatively demonstrates that PICNIC can accurately capture 1D spherical hydrodynamics and burn propagation and similarly captures the anisobaric dynamics of the burn wave. The main discrepancy with HYDRA is delayed bangtime and a ∼20% higher peak hotspot temperature,

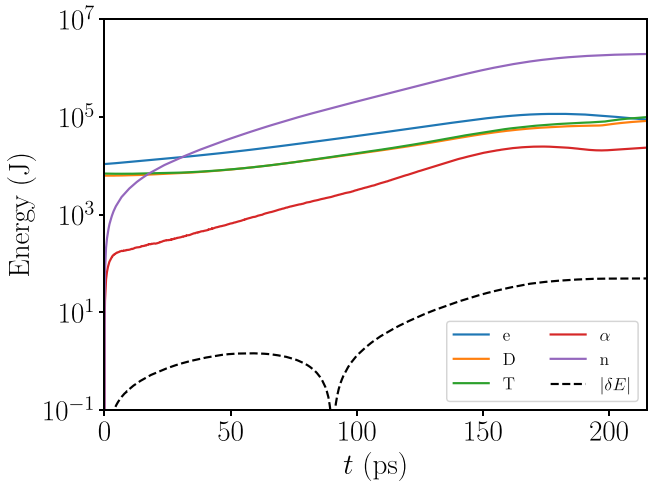

FIG. 4. Total kinetic energy of each major species (including particles that have left the simulation domain) and the numerical energy conservation violation δE of simulation (ii), which is representative of all three simulations.

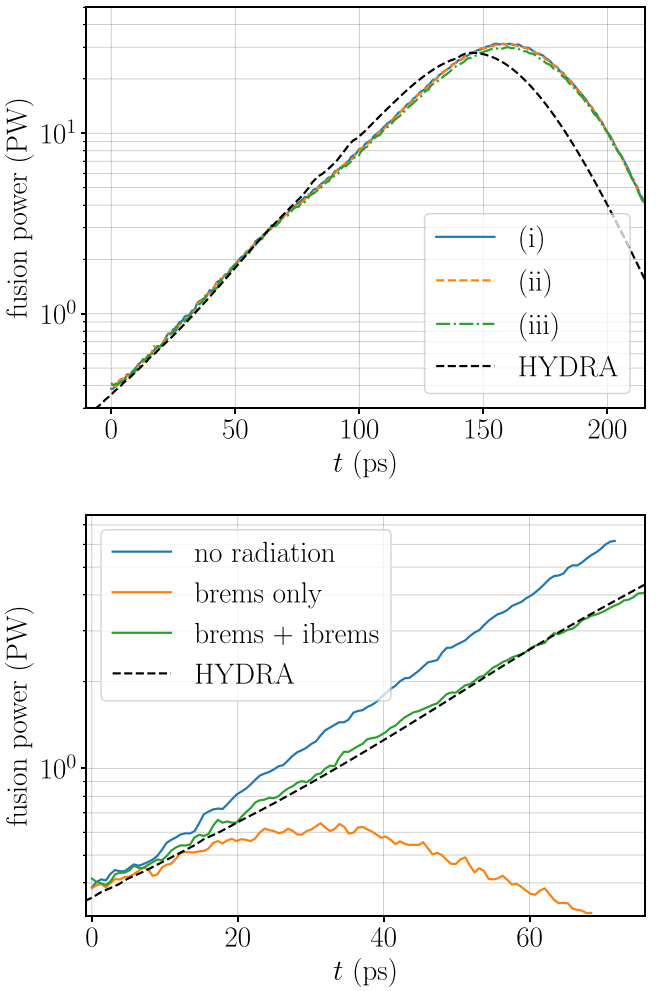

FIG. 5. (Top) Fusion energy production rate comparison between PICNIC and HYDRA. (Bottom) Early-time production rates of reruns of simulation (ii), one with no radiation physics and the other with bremsstrahlung emission, but no absorption.

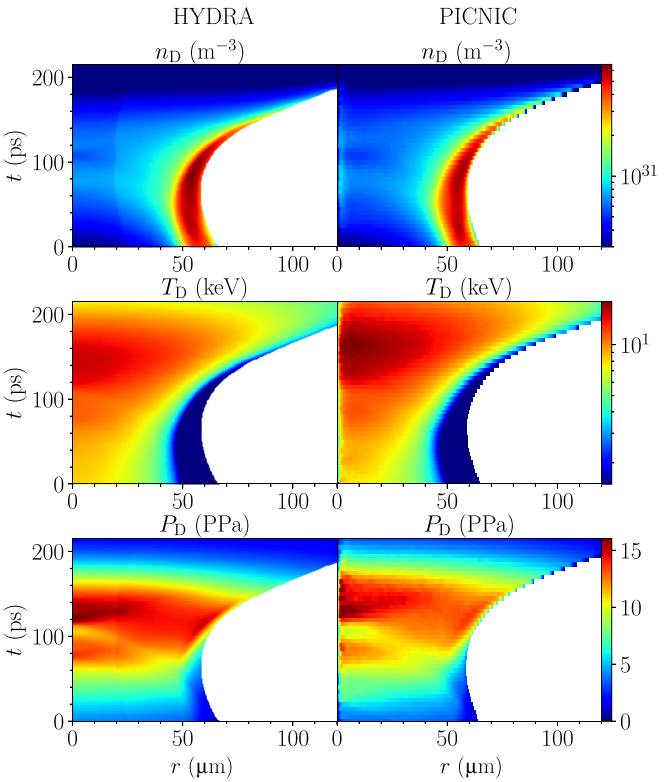

FIG. 6. Comparison of deuterium density, temperature, and pressure phase-space plots between PICNIC simulation (i) and HYDRA.

which is associated with the aforementioned increased yield prediction.

The resulting neutron spectra are shown in Fig. 7. For the shallow-angle cumulative Coulomb only case (i), we can see the TBN contribution to the high-energy neutron distribution, which is small relative to the AKN RIFs seen in cases (ii) and (iii). We do not see a notable difference in the D–D and T–T spectra apart from an increased broadening at the high end of the T–T spectrum due to RIFs. The 15.5–18 MeV AKN spectra from simulations (i) and (ii) are similar to those found in experiments at the NIF [16]. Above 18 MeV, the NKN signal in the experiment begins to dominate, which was not included in our simulations. Markedly, there are no significant differences in the AKN spectra between cases (ii) and (iii), which is expected as D–T fusion is only slightly anisotropic in this reactant energy range, as shown in Fig. 2. The D–T anisotropy is only envisioned to influence the high-energy 18–30 MeV NKN signal in experiments.

Shifting our attention to the spectral shift vs temperature plots, at early times around stagnation, the spectral shift hovers slightly above the Maxwellian locus. This suggests that non-Maxwellian distributions, apart from producing knock-on neutrons, also play a role in the burn itself. However, at bangtime and onward the Doppler shifts from the hydrodynamic explosion widen the accumulated neutron spectrum such that it ends up well below the curve. Notably, we do not see this behavior change with the inclusion of large-angle scattering physics nor anisotropic fusion, and at no point in the simulations do the spectral shifts approach the anomalous >50 keV shift measured experimentally for shot N210808, as reported in [5].

Snapshots of the energy spectra of the charged species at bangtime are shown in Fig. 8 to demonstrate the generation of suprathermal fuel ions via large-angle NES collisions with alphas, and its mediation by stopping against the bulk e/D/T plasma. The suprathermal D/T tail is similar to our previous 0D benchmarks for the generalized Coulomb method with large-angle Rutherford scattering [25], but with a larger population relative to the alphas due to the inclusion of NES necessary to model AKN. Also present are the effects of large-angle Rutherford scattering on the minor species p and ^{3}He, which receive small high-energy tails above their D–D fusion birth energies. The small proton peak around 14.7 MeV is from D ^{3}He fusion. For the shallow-angle cumulative Coulomb-only case, there is still a source of suprathermal tritons from D–D fusion that produces TBN.

V. CONCLUSION

We have presented results from 1D spherical simulations of the entire burnwave of the NIF shot N210808 using the code PICNIC, which treats all species fully kinetically with accurate masses, fields, and scattering physics. This numerical tool allows us to study the kinetic effects involved in ignition, which are expected to become increasingly important with higher achieved yields, where the suprathermal fusion products become a significant fraction of the total mass.

With the inclusion of large-angle Rutherford and NES physics, we have recovered the well-known AKN RIF spectrum with this self-consistent, fully kinetic PIC code. However, despite having all the large-angle scattering physics necessary to produce the experimentally observed RIFs, we do not observe any large increase in the spectral shift of the D–T primary spectrum as was measured in [4,5]. This rules out kinetic effects in 1D axisymmetric geometry with large-angle collisions as an explanation for the anomalous shift, which contrasts with the findings of a previous PIC study [53]. Since 2D kinetic effects involving self-generated magnetic fields have not been ruled out, we plan to conduct simulations in RZ geometry in the future to investigate their impact on the burnwave and neutron spectrum. Kinetic effects associated with dopants or impurities in the fuel region, especially in the burning plasma regime where NES with alphas can generate suprathermal impurity ions, are also subject for the future study.

ACKNOWLEDGMENTS

This work was performed under the auspices of the U.S. Department of Energy by Lawrence Livermore National Laboratory under Contract No. DE-AC52-07NA27344 and was supported by the LLNL-LDRD Program under Project No. 23-ERD-007. Document release No. LLNL-JRNL-2006642.

DATA AVAILABILITY

The data that support the findings of this article are not publicly available upon publication because it is not

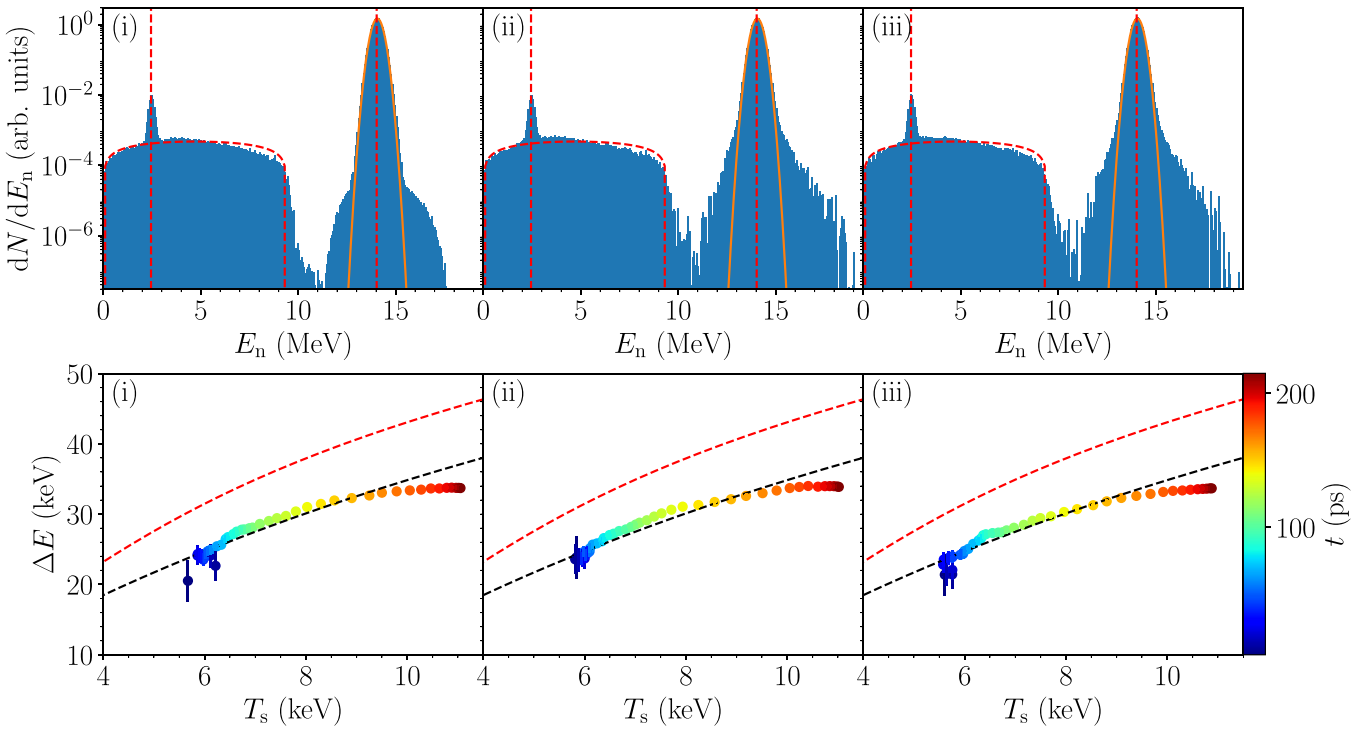

FIG. 7. (Top) Total accumulated at-birth neutron spectra. The vertical red dashed lines indicate the D–D and D–T fusion neutron energies in the zero reactant energy limit $E_{0,\mathrm{D–D}} = 2.4487\,\mathrm{MeV}$, $E_{0,\mathrm{D–T}} = 14.0284\,\mathrm{MeV}$ [42]. Similarly, the red dashed region indicates the T–T fusion neutron spectrum at zero reactant energy without accounting for the neutron-neutron interaction. The solid orange curve is a fitted Gaussian to the D–T primary peak using the FWHM to set the variance, i.e., $\mathrm{Var}(E_n) = \mathrm{FWHM}/(8\ln 2)$. (Bottom) Spectral shift vs spectral temperature of the accumulated D–T primary neutron spectrum over time. The black and red dashed lines indicate the Maxwellian locus and the isotropic upper limit, respectively. Error bars indicate the uncertainty due to low neutron macroparticle statistics at early times. The spectral temperature here is also inferred from the FWHM of the D–T primary peak.

technically feasible and/or the cost of preparing, depositing, and hosting the data would be prohibitive within the terms of this research project. The data are available from the authors upon reasonable request.

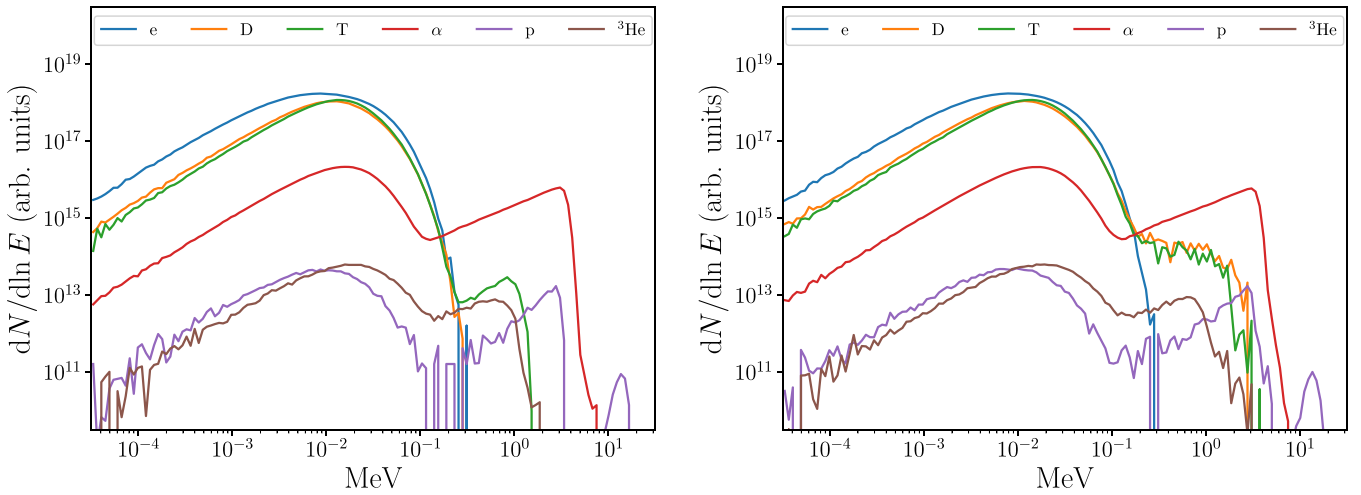

FIG. 8. Snapshots at bangtime of the energy spectra of all charged species in the fuel region for simulation (i) (left) with cumulative Coulomb scattering only and (ii) (right) with cumulative Coulomb, large-angle Rutherford, and α–D/α–T NES. The spectra from simulation (iii) (not presented) are very similar to those from (ii).

[1] A. B. Zylstra, O. A. Hurricane, D. A. Callahan, A. L. Kritcher, J. E. Ralph, H. F. Robey, J. S. Ross, C. V. Young, K. L. Baker, and D. T. Casey, Burning plasma achieved in inertial fusion, Nature (London) **601**, 542 (2022).

[2] A. B. Zylstra, A. L. Kritcher, O. A. Hurricane, D. A. Callahan, J. E. Ralph, D. T. Casey, A. Pak, O. L. Landen, B. Bachmann, K. L. Baker, L. B. Hopkins, S. D. Bhandarkar, J. Biener, R. M. Bionta, N. W. Birge, T. Braun, T. M. Briggs, P. M. Celliers, H. Chen, C. Choate *et al.*, Experimental achievement and signatures of ignition at the national ignition facility, Phys. Rev. E **106**, 025202 (2022).

[3] H. Abu-Shawareb *et al.*, Achievement of target gain larger than unity in an inertial fusion experiment, Phys. Rev. Lett. **132**, 065102 (2024).

[4] E. P. Hartouni, A. S. Moore, A. J. Crilly, B. D. Appelbe, P. A. Amendt, K. L. Baker, D. T. Casey, D. S. Clark, T. Döppner, and M. J. Eckart, Evidence for suprathermal ion distribution in burning plasmas, Nat. Phys. **19**, 72 (2023).

[5] A. S. Moore, D. J. Schlossberg, B. D. Appelbe, G. A. Chandler, A. J. Crilly, M. J. Eckart, C. J. Forrest, V. Y. Glebov, G. P. Grim, E. P. Hartouni, R. Hatarik, S. M. Kerr, J. Kilkenny, and J. P. Knauer, Neutron time of flight (nToF) detectors for inertial fusion experiments, Rev. Sci. Instrum. **94**, 061102 (2023).

[6] D. Ryutov, Energetic ion population formed in close collision with fusion alpha-particles, Phys. Scr. **45**. 153 (1992).

[7] P. Helander, M. Lisak, and D. D. Ryutov, Formation of hot ion populations in fusion plasmas by close collisions with fast particles, Plasma Phys. Controlled Fusion **35**, 363 (1993).

[8] R. K. Fisher, P. B. Parks, J. M. McChesney, and M. N. Rosenbluth, Fast alpha particle diagnostics using knock-on ion tails, Nucl. Fusion **34**, 1291 (1994).

[9] L. Ballabio, G. Gorini, and J. Källne, α-particle knock-on signature in the neutron emission of DT plasmas, Phys. Rev. E **55**, 3358 (1997).

[10] J. Källne, L. Ballabio, J. Frenje, S. Conroy, G. Ericsson, M. Tardocchi, E. Traneus, and G. Gorini, Observation of the alpha particle "knock-on" neutron emission from magnetically confined DT fusion plasmas, Phys. Rev. Lett. **85**, 1246 (2000).

[11] A. A. Korotkov, A. Gondhalekar, and R. J. Akers, Observation of MeV energy deuterons produced by knock-on collisions between deuterium–tritium fusion α-particles and plasma fuel ions, Phys. Plasmas **7**, 957 (2000).

[12] H. Matsuura and Y. Nakao, Effect of nuclear elastic scattering on ion heating characteristics in deuterium-tritium thermonuclear plasmas, Phys. Plasmas **13**, 062507 (2006).

[13] H. Matsuura and Y. Nakao, Distortion of bulk-ion distribution function due to nuclear elastic scattering and its effect on $\mathrm{T}(d,n)^4\mathrm{He}$ reaction rate coefficient in neutral-beam-injected deuterium-tritium plasmas, Phys. Plasmas **14**, 054504 (2007).

[14] F. S. Zaitsev, A. Gondhalekar, T. J. Johnson, S. E. Sharapov, D. S. Testa, I. I. Kurbet, and J. E. contributors, Suprathermal deuterium ions produced by nuclear elastic scattering of ICRH driven He^3 ions in JET plasmas, Plasma Phys. Control. Fusion **49**, 1747 (2007).

[15] A. C. Hayes, G. Jungman, A. E. Schulz, M. Boswell, M. M. Fowler, G. Grim, A. Klein, R. S. Rundberg, J. B. Wilhelmy, and D. Wilson, Reaction-in-flight neutrons as a test of stopping power in degenerate plasmas, Phys. Plasmas **22**, 082703 (2015).

[16] J. Jeet, B. D. Appelbe, A. J. Crilly, L. Divol, M. Eckart, K. D. Hahn, E. P. Hartouni, A. Hayes, S. Kerr, and Y. Kim, Diagnosing up-scattered deuterium–tritium fusion neutrons produced in burning plasmas at the national ignition facility, Rev. Sci. Instrum. **95**, 093521 (2024).

[17] M. G. Johnson, D. Schlossberg, B. Appelbe, J. Ball, M. Bitter, D. T. Casey, A. Celora, L. Ceurvorst, H. Chen, and S. Conroy, Learning from each other: Cross-cutting diagnostic development activities between magnetic and inertial confinement fusion, Rev. Sci. Instrum. **95**, 093533 (2024).

[18] O. Larroche, Kinetic simulations of fuel ion transport in ICF target implosions, Eur. Phys. J. D **27**, 131 (2003).

[19] O. Larroche, H. G. Rinderknecht, and M. J. Rosenberg, Nuclear yield reduction in inertial confinement fusion exploding-pusher targets explained by fuel-pusher mixing through hybrid kinetic-fluid modeling, Phys. Rev. E **98**, 031201(R) (2018).

[20] W. T. Taitano, B. D. Keenan, L. Chacón, S. E. Anderson, H. R. Hammer, and A. N. Simakov, An Eulerian Vlasov-Fokker–Planck algorithm for spherical implosion simulations of inertial confinement fusion capsules, Comput. Phys. Commun. **263**, 107861 (2021).

[21] O. M. Mannion, W. T. Taitano, B. D. Appelbe, A. J. Crilly, C. J. Forrest, V. Y. Glebov, J. P. Knauer, P. W. McKenty, Z. L. Mohamed, C. Stoeckl, B. D. Keenan, J. P. Chittenden, P. Adrian, J. Frenje, N. Kabadi, M. G. Johnson, and S. P. Regan, Evidence of non-Maxwellian ion velocity distributions in spherical shock-driven implosions, Phys. Rev. E **108**, 035201 (2023).

[22] J. R. Angus, W. Farmer, A. Friedman, D. Ghosh, D. Grote, D. Larson, and A. Link, An implicit particle code with exact energy and charge conservation for electromagnetic studies of dense plasmas, J. Comput. Phys. **491**, 112383 (2023).

[23] J. R. Angus, W. Farmer, A. Friedman, V. Geyko, D. Ghosh, D. Grote, D. Larson, and A. Link, An implicit particle code with exact energy and charge conservation for studies of dense plasmas in axisymmetric geometries, J. Comput. Phys. **519**, 113427 (2024).

[24] J. R. Angus, Y. Fu, V. Geyko, D. Grote, and D. Larson, Moment-preserving Monte-Carlo Coulomb collision method for particle codes, J. Comput. Phys. **531**, 113927 (2025).

[25] J. R. Angus and J. J. van de Wetering, A binary collision method for screened Coulomb collisions in weakly and moderately coupled plasmas, arXiv:2504.14067.

[26] A. V. Bobylev and I. Potapenko, Monte Carlo methods and their analysis for Coulomb collisions in multicomponent plasmas, J. Comput. Phys. **246**, 123 (2013).

[27] A. E. Turrell, M. Sherlock, and S. J. Rose, Self-consistent inclusion of classical large-angle Coulomb collisions in plasma Monte Carlo simulations, J. Comput. Phys. **299**, 144 (2015).

[28] J. Lindhard and A. H. Sørensen, Relativistic theory of stopping for heavy ions, Phys. Rev. A **53**, 2443 (1996).

[29] C.-K. Li and R. D. Petrasso, Fokker-Planck equation for moderately coupled plasmas, Phys. Rev. Lett. **70**, 3063 (1993).

[30] J. Lindl, O. Landen, J. Edwards, E. Moses, and N. I. C. Team, Review of the national ignition campaign 2009-2012, Phys. Plasmas **21**, 020501 (2014).

[31] B. L. Reichelt, R. D. Petrasso, and C. Li, Effects of alpha-ion stopping on ignition and ignition criteria in inertial confinement fusion experiments, Phys. Plasmas **31**, 010702 (2024).

[32] J. Eriksson, S. Conroy, E. A. Sundén, and C. Hellesen, Calculating fusion neutron energy spectra from arbitrary reactant distributions, Comput. Phys. Commun. **199**, 40 (2016).

[33] D. A. Brown, M. B. Chadwick, R. Capote, A. C. Kahler, A. Trkov, M. W. Herman, A. A. Sonzogni, Y. Danon, A. D. Carlson, and M. Dunn, ENDF/B-VIII. 0: The 8th major release of the nuclear reaction data library with CIELO-project cross sections, new standards, and thermal scattering data, Nucl. Data Sheets **148**, 1 (2018).

[34] M. J. Lavell, A. J. Kish, A. T. Sexton, E. S. Evans, I. Mohammad, S. Gomez-Ramirez, W. Scullin, M. Borscz, S. Pikuz, and T. A. Mehlhorn, A kinetic study of fusion burn waves in compressed deuterium–tritium and proton–boron plasmas, Front. Phys. **12**, 1440037 (2024).

[35] S. M. Seltzer and M. J. Berger, Bremsstrahlung energy spectra from electrons with kinetic energy 1 keV–10 GeV incident on screened nuclei and orbital electrons of neutral atoms with Z = 1–100, At. Data Nucl. Data Tables **35**, 345 (1986).

[36] A. Okhrimovskyy, A. Bogaerts, and R. Gijbels, Electron anisotropic scattering in gases: A formula for Monte Carlo simulations, Phys. Rev. E **65**, 037402 (2002).

[37] H.-S. Bosch and G. M. Hale, Improved formulas for fusion cross-sections and thermal reactivities, Nucl. Fusion **32**, 611 (1992).

[38] D. P. Higginson, A. Link, and A. Schmidt, A pairwise nuclear fusion algorithm for weighted particle-in-cell plasma simulations, J. Comput. Phys. **388**, 439 (2019).

[39] B. Lacina, J. Ingley, and D. W. Dorn, Neutron-neutron interaction in the T + T reaction, Technical Report, Lawrence Radiation Laboratory, University of California, Livermore (1965), available at: https://www.osti.gov/biblio/4559707.

[40] D. T. Casey, J. A. Frenje, M. G. Johnson, M. J.-E. Manuel, N. Sinenian, A. B. Zylstra, F. H. Séguin, C. K. Li, R. D. Petrasso, V. Y. Glebov, P. B. Radha, D. D. Meyerhofer, T. C. Sangster, D. P. McNabb, P. A. Amendt, R. N. Boyd, S. P. Hatchett, S. Quaglioni, J. R. Rygg, I. J. Thompson *et al.*, Measurements of the $T(t, 2n)^4He$ neutron spectrum at low reactant energies from inertial confinement implosions, Phys. Rev. Lett. **109** (2012) 025003.

[41] H. Brysk, Fusion neutron energies and spectra, Plasma Phys. **15**, 611 (1973).

[42] A. J. Crilly, B. D. Appelbe, O. M. Mannion, W. Taitano, E. P. Hartouni, A. S. Moore, M. Gatu-Johnson, and J. P. Chittenden, Constraints on ion velocity distributions from fusion product spectroscopy, Nucl. Fusion **62**, 126015 (2022).

[43] L. Ballabio, J. Källne, and G. Gorini, Relativistic calculation of fusion product spectra for thermonuclear plasmas, Nucl. Fusion **38**, 1723 (1998).

[44] H. Azechi, M. D. Cable, and R. O. Stapf, Review of secondary and tertiary reactions, and neutron scattering as diagnostic techniques for inertial confinement fusion targets, Laser Part. Beams **9**, 119 (1991).

[45] D. B. Sayre, C. R. Brune, J. A. Caggiano, V. Y. Glebov, R. Hatarik, A. D. Bacher, D. L. Bleuel, D. T. Casey, C. J. Cerjan, M. J. Eckart, R. J. Fortner, J. A. Frenje, S. Friedrich, M. Gatu-Johnson, G. P. Grim, C. Hagmann, J. P. Knauer, J. L. Kline, D. P. McNabb, J. M. McNaney *et al.*, Measurement of the T + T neutron spectrum using the national ignition facility, Phys. Rev. Lett. **111** (2013) 052501 .

[46] M. G. Johnson, C. Forrest, D. Sayre, A. Bacher, J.-L. Bourgade, C. Brune, J. Caggiano, D. Casey, J. Frenje, V. Glebov, G. Hale, R. Hatarik, H. Herrmann, R. Janezic, Y. Kim, J. Knauer, O. Landoas, D. McNabb, M. Paris, R. Petrasso *et al.*, Experimental evidence of a variant neutron spectrum from the *T(t,2n)α* reaction at center-of-mass energies in the range of 16–50 keV, Phys. Rev. Lett. **121** (2018) 042501.

[47] N. Otuka and M. Drosg, Evaluation of the absolute angle-dependent differential neutron production cross sections by the reactions 3H(p,n)3He, 1H(t,n)3He, 2H(d,n)3He, 3H(d,n)4He, and 2H(t,n)4He and of the cross sections of their time-reversed counterparts up to 30 MeV and beyond, Technical Report, NA (2015), URL: https://www-nds.iaea.org/publications/indc/indc-aus-0019/.

[48] A. L. Kritcher, C. V. Young, H. F. Robey, C. R. Weber, A. B. Zylstra, O. A. Hurricane, D. A. Callahan, J. E. Ralph, J. S. Ross, and K. L. Baker, Design of inertial fusion implosions reaching the burning plasma regime, Nat. Phys. **18**, 251 (2022).

[49] A. L. Kritcher, A. B. Zylstra, C. R. Weber, O. A. Hurricane, D. A. Callahan, D. S. Clark, L. Divol, D. E. Hinkel, K. Humbird, O. Jones, J. D. Lindl, S. Maclaren, D. J. Strozzi, C. V. Young, A. Allen, B. Bachmann, K. L. Baker, T. Braun, G. Brunton, D. T. Casey *et al.*, Design of the first fusion experiment to achieve target energy gain G > 1, Phys. Rev. E **109** (2024) 025204.

[50] G. Maynard and C. Deutsch, Born random phase approximation for ion stopping in an arbitrarily degenerate electron fluid, J. Phys. France **46**, 1113 (1985).

[51] W. Daughton, B. J. Albright, S. M. Finnegan, B. M. Haines, J. L. Kline, J. P. Sauppe, and J. M. Smidt, Influence of mass ablation on ignition and burn propagation in layered fusion capsules, Phys. Plasmas **30**, 012704 (2023).

[52] B. J. Albright, W. Daughton, B. M. Haines, N. M. Hoffman, J. J. Kuczek, R. Lester, K. D. Meaney, and J. P. Sauppe, Use of tritium-rich fuel to improve the yield of layered deuterium/tritium inertial fusion capsules, High Energy Density Phys. **52**, 101118 (2024).

[53] Y. Xue, D. Wu, and J. Zhang, Mechanisms behind the surprising observation of supra-thermal ions in NIF's fusion burning plasmas, Sci. Bull. **70**, 359 (2025).